Research Square

Preprints are preliminary reports that have not undergone peer review.
They should not be considered conclusive, used to inform clinical practice,
or referenced by the media as validated information.

3D Snapshot of Ultrafast Terahertz Electromagnetic Wave Packets

Zhengyan Li

zhengyanli@hust.edu.cn

Huazhong University of Science and Technology https://orcid.org/0000-0001-8935-8727

Yaodan Hu

Huazhong University of Science and Technology https://orcid.org/0009-0007-2066-3660

Yisen Zhang

Huazhong University of Science and Technology

Jiapeng Li

Huazhong University of Science and Technology

Fan Xia

Huazhong University of Science and Technology

Changda Peng

Huazhong University of Science and Technology

Kuanjun Fan

Huazhong University of Science and Technology

Ping Li

Laser Fusion Research Center, Chinese Academy of Engineering Physics

Article

Keywords:

Posted Date: November 24th, 2026

DOI: https://doi.org/10.21203/rs.3.rs-11013810/v1

License: This work is licensed under a Creative Commons Attribution 4.0 International License.
Read Full License

Additional Declarations: There is **NO** Competing Interest.

3D Snapshot of Ultrafast Terahertz Electromagnetic Wave Packets

Yaodan Hu[1,2], Yisen Zhang[1], Jiapeng Li[2], Fan Xia[1], Changda Peng[2], Ping Li[3*], Kuanjun Fan[2*], Zhengyan Li[1#]

1. Wuhan National Laboratory for Optoelectronics, Huazhong University of Science and Technology, Wuhan, Hubei, China

2. School of Electrical and Electronic Engineering, Huazhong University of Science and Technology, Wuhan, Hubei, China

3. Laser Fusion Research Center, Chinese Engineering Physics Academy, Mianyang, Sichuan, China

Corresponding email: zhengyanli@hust.edu.cn, kjfan@hust.edu.cn, liping1984@caep.cn

Abstract

Optics and photonics study the sciences of electromagnetic waves, which were well formulated by Maxwell's equations more than 160 years ago. However, surprisingly, the fundamental problem of experimentally measuring an electromagnetic wave with all necessary electric field information in one go is yet to be realized. Instead, only limited physical quantities describing an optical wave can be picked out and measured, such as intensity, phase, spectrum, polarization, and their spatial or/and temporal profile. Here we demonstrate a single-shot three-dimensional (3D) spatiotemporal visualization of an electromagnetic wave packet in the terahertz (THz) spectral regime, unveiling complete spatiotemporal properties of light, including the three complete electric field components E_x, E_y and E_z, and their carrier-envelope phases. To capture such a 3D snapshot, the THz wave packet information is imprinted in a whole on a chirped ultrafast near-infrared probe laser pulse through electro-optic sampling, and extracted from the optical probe via a proposed technique of single-shot full-Stokes compressive spatiospectral polarimetry. 3D snapshots of electromagnetic wave packets not only solve the fundamental problem of seeing the traveling wave solution to Maxwell's equations, but also open the door to holistic optical wave sensing.

Main

Maxwell's 1865 masterpiece "A dynamical theory of the electromagnetic field" predicted electromagnetic waves propagating in vacuum at the speed of light c [1], not only laying the very cornerstone of the Second Industrial Revolution, but also specifically paving the way for optics and photonics. Experimentally measuring an electromagnetic wave with its complete 3D spatiotemporal distribution of field strength and polarizing direction in a single exposure is thus a fundamental problem yet to be solved. For example, in the visible or infrared spectral regime, the 3D spatiotemporal profile of amplitude, phase, and polarization of an ultrafast vectorial laser field has been characterized in single-shot [2,3], whereas the measured phase is only related to the laser complex amplitude envelope rather than the waveform [4]. The waveform of an ultrafast laser pulse has been measured only in the temporal domain without any spatial or polarization information, either in multi-shot based on electro-optical sampling [5-7], attosecond streak camera [8,9], tunneling ionization gating [10,11], or in single-shot due to field-induced carrier excitation in solids [12,13].

For the THz radiation, it has applications including free-space communication [14,15], security and biomedical imaging [16,17], carrier dynamics spectroscopy [18,19], and particle acceleration [20,21]. A THz wave packet snapshot manifested by 3D spatiotemporal field strength and direction profiles delivers the most holistic electromagnetic wave information in a single shot, but it is technically challenging. Using a two-dimensional photoconductive antenna array, the 3D field strength profile of a linearly polarized THz pulse can be measured in multiple shots by scanning the optical probe time delay [22,23]. Electro-optic sampling by a synchronized optical probe has long been applied to measure the temporal THz field strength profile [24], even in single-shot [25-28], but additionally multiple exposures are required to implement spatial information [29,30]. Genuine single-shot 3D spatiotemporal THz field strength visualizations have been achieved by encoding the temporal information into the spatial frequency k-space [31,32], whereas the approach is only applicable to linearly polarized THz pulses without field direction variations.

To display the vectorial nature of an electromagnetic wave, the THz field direction,

or the polarization, is also expected to be spatiotemporally resolved; however, so far only the one-dimensional temporal field direction characterization is available. For example, polarization-sensitive photoconductive antenna detection of a THz pulse is enabled by multi-contact receivers [33,34]. In the electro-optical sampling scheme, the field direction is resolved by rotating polarization-sensitive THz optics in multiple measurements [35-37]. However, the time-dependent field direction profiles in all the above studies have to be obtained in multiple shots by scanning the optical probe time delay. Single-shot temporal field direction measurement has been achieved recently by applying a chirped and stretched optical probe which samples the THz field-induced transient birefringence in an electro-optical medium [38,39]. Spatially resolved THz field direction measurements have also been attempted [40,41], but by scanning the detection position with a point-wise detector in multi-shot.

In this article, we have demonstrated single-shot 3D spatiotemporal visualization of an ultrafast electromagnetic wave packet in the THz spectral regime, based on the developed single-shot full-Stokes compressive spatiospectral polarimetry of the chirped optical probe, which electro-optically samples the THz wave packet. One can uniquely and robustly reconstruct the 3D spatiotemporal profiles of the THz electric field components along all directions from the measured 3D spatial-spectral Stokes parameter profiles of the optical probe. Therefore, fundamental properties of an electromagnetic wave interacting with matter, such as longitudinal field components, carrier-envelope phase shift in a dispersive medium, and polarization modification in a birefringent crystal, are unveiled.

Principles of the 3D spatiotemporal THz electromagnetic wave packet snapshot and the single-shot compressive spatiospectral polarimetry

A THz electromagnetic wave packet undergoing paraxial propagation along the z-direction is comprehensively described by 3D spatiotemporal profiles of the transverse electric field components $E_x(x,y,t)$ and $E_y(x,y,t)$, as well as the longitudinal electric field strength $E_z(x,y,t)$, so the vectorial total field is

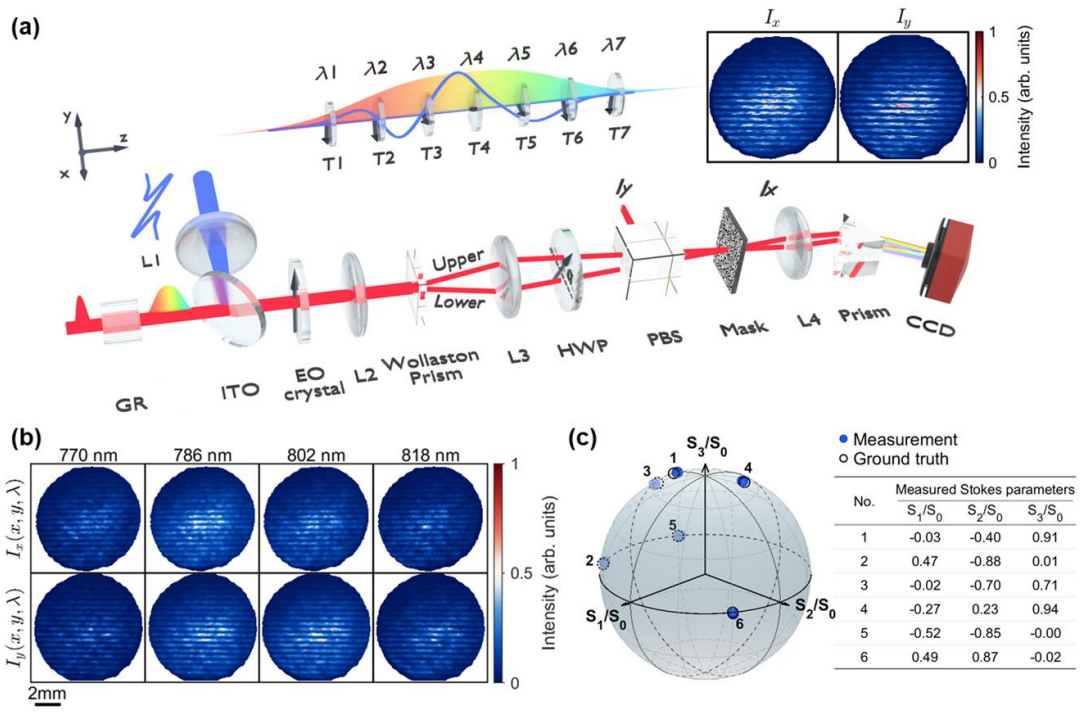
$$\mathbf{E}(x,y,t) = E_x(x,y,t)\hat{\boldsymbol{x}} + E_y(x,y,t)\hat{\boldsymbol{y}} + E_z(x,y,t)\hat{\boldsymbol{z}}. \quad (1)$$

Here, the z-dependence of these 3D profiles is not explicitly presented as $\partial_z = -c^{-1}\partial_t$ for a traveling wave packet, and the Poisson equation linking the transverse and longitudinal field profiles becomes $c^{-1}\partial_t E_z = \partial_x E_x + \partial_y E_y$.

The electro-optic sampling scheme is applied to capture a single-shot snapshot of the complete THz wave packet $\mathbf{E}(x, y, t)$. As shown in Figure 1a inset, the THz wave packet induces a transient effective wave plate in the electro-optic (EO) crystal, with the optical axis angle of $\psi = \tan^{-1}\left(\sqrt{1 + E_y^2/4E_x^2} - E_y/2E_x\right)$ and the phase retardation of $\Delta = -(\pi n_o^3 L r/\lambda_0)E_x\sqrt{4 + E_y^2/E_x^2}$ [42], where n_0, L, r are the refractive index, the thickness, the electro-optic coefficient of the electro-optic crystal respectively, and λ_0 is the central wavelength of a probing laser pulse (Detailed derivations see Supplementary Document, Section 1). The optical probe is generated by introducing a linear chirp (the chirp rate a_λ) to a femtosecond laser pulse and stretching its pulse duration to spatiotemporally overlap it with the THz wave packet. The chirped optical probe experiences the transient effective wave plate at different times t, so the polarization states of the corresponding wavelength components $\lambda = \lambda_0 + t/a_\lambda$ are transformed according to [43,44]

$$\begin{bmatrix} S_1^{(\mathrm{Out})}/S_0^{(\mathrm{Out})} \\ S_2^{(\mathrm{Out})}/S_0^{(\mathrm{Out})} \\ S_3^{(\mathrm{Out})}/S_0^{(\mathrm{Out})} \end{bmatrix} = \begin{bmatrix} \cos^2 2\psi + \sin^2 2\psi \cos\Delta & \cos 2\psi \sin 2\psi\,(1 - \cos\Delta) & -\sin 2\psi \sin\Delta \\ \cos 2\psi \sin 2\psi\,(1 - \cos\Delta) & \sin^2 2\psi + \cos^2 2\psi \cos\Delta & \cos 2\psi \sin\Delta \\ \sin 2\psi \sin\Delta & -\cos 2\psi \sin\Delta & \cos\Delta \end{bmatrix} \begin{bmatrix} S_1^{(\mathrm{In})}/S_0^{(\mathrm{In})} \\ S_2^{(\mathrm{In})}/S_0^{(\mathrm{In})} \\ S_3^{(\mathrm{In})}/S_0^{(\mathrm{In})} \end{bmatrix} \quad (2)$$

Here $S_i^{(\mathrm{In})}$ and $S_i^{(\mathrm{Out})}$ $(i = 0, 1, 2, 3)$ are the full-Stokes polarization states of the optical probe before and after interacting with the THz wave packet within the electro-optic crystal (Detailed derivations see Supplementary Document, Section 1). Once the 3D spatiospectral full-Stokes polarization state profile of the optical probe is measured in a single shot, the 3D spatiotemporal snapshot of the THz wave packet $\mathbf{E}(x, y, t)$ can be reconstructed.



No.	Measured Stokes parameters		
	S_1/S_0	S_2/S_0	S_3/S_0
1	-0.03	-0.40	0.91
2	0.47	-0.88	0.01
3	-0.02	-0.70	0.71
4	-0.27	0.23	0.94
5	-0.52	-0.85	-0.00
6	0.49	0.87	-0.02

Figure 1. Principle of single-shot compressive spatiospectral polarimetry and a 3D spatiotemporal snapshot of a vectorial THz electromagnetic wave packet. a. Schematic of the experimental setup. A temporally chirped near-infrared probe pulse samples the THz electric field in a ZnTe electro-optic (EO) crystal, mapping the 3D spatiotemporal THz wave packet onto the spatiospectral full-Stokes polarization states of the probe laser pulse, which is chirped by a glass rod (GR) and combined by an indium tin oxide (ITO) coated glass plate. The polarization-modulated probe transmits through a Wollaston prism, a half-wave plate (HWP), a polarizer beam splitter (PBS), a spatially encoding mask, an angularly dispersive prism, and a charge coupled device (CCD) camera for the 3D spatiospectral interferogram $I_x(x,y,\lambda)$ measurement. The probe laser pulse reflected from PBS is for $I_y(x,y,\lambda)$ measurement. **b**. The reconstructed 3D spatiospectral interferograms $I_x(x,y,\lambda)$ and $I_y(x,y,\lambda)$ at four representative wavelengths of 770, 786, 802, and 818 nm. **c**. Measured Stokes parameters (solid dots) of different probe laser polarization states compared to ground-truth values (circles), when the pump is absent.

Therefore, we propose a novel technique of single-shot full-Stokes compressive spatiospectral polarimetry for the chirped optical probe. Figure 1a depicts the schematic diagram of the experimental setup. A femtosecond probe laser pulse (central wavelength $\lambda_0 = 800$ nm, temporal duration 33 fs) transmits through chirp media (a 3-cm thick SF11 glass rod and a 9-cm thick ZF13 glass rod, $a_\lambda = 69$ fs/nm) and is temporally stretched to 1.6 ps. The chirped probing pulse is combined by an indium tin oxide (ITO, 30 Ω/sq) coated glass plate with the THz wave packet, which is generated

through tilted-pulse-front optical rectification in a $LiNbO_3$ crystal [45] and focused by a lens L1 (focal length 75 mm) onto a 1-mm-thick ZnTe electro-optical crystal (see Method, Section 1). In the crystal, the 3D THz wave packet $\mathbf{E}(x, y, t)$ modulates the spatiospectral polarization state $S_i(x, y, \lambda = \lambda_0 + t/a_\lambda)$ $(i = 0, 1, 2, 3)$ of the optical probe.

The polarization-modulated optical probe is first imaged by a lens L2 to a Wollaston prism, which separates *x*- and *y*-polarized components of the optical probe with a small angle δ =8.7 mrad. The *x*- and *y*-polarized optical probe components are imaged by another lens L3 (magnification $M = 5$) to the detection plane along the upper and lower paths, respectively, and a half-wave plate (HWP) and a polarization beam splitter (PBS) are placed between the lens L3 and the detection plane. The optical axis angle of the half-wave plate (HWP) is $\alpha = 30°$ and rotates the polarization directions of probe pulses in both the upper and lower paths by $2\alpha = 60°$. The *x*-polarized components of probe pulses in the upper and lower paths transmit through the PBS and reunite on the detection plane with an angle of δ/M, generating a 3D spatiospectral interferogram $I_x(x, y, \lambda)$ for all wavelengths λ with the corresponding fringe period of $\Lambda = \lambda M/\delta$.

The 3D interferogram is highly sparse and obtained in single-shot using a compressive spectral intensity imaging method [46]: it is spatially modulated by an encoding mask (a random binary grid pattern formed by coating chromium on a glass plate), imaged by a positive lens L4, spectrally dispersed by a prism, captured by a charge-coupled device (CDD) camera, and computationally reconstructed using a compressive sensing algorithm of TwIST [47] (See Method, Section 2). Similarly, the *y*-polarized components of probe pulses in the upper and lower paths are reflected from the PBS, thereby producing the 3D spatiospectral interferogram $I_y(x, y, \lambda)$ as well (Fig 1b). Now the 3D spatiospectral Stokes parameter profiles S_i/S_0 $(i = 1,2,3)$ of the probing laser pulse are linked to the 3D interferograms I_x and I_y through (Detailed derivations see Supplementary Document, Section 2)

$$\begin{cases} I_x = \frac{1}{2}[S_0 + S_1 \cos 4\alpha] + \frac{1}{2}\sin 4\alpha \left[S_2 \cos\frac{2\pi y}{\Lambda} - S_3 \sin\frac{2\pi y}{\Lambda}\right] \\ I_y = \frac{1}{2}[S_0 - S_1 \cos 4\alpha] - \frac{1}{2}\sin 4\alpha \left[S_2 \cos\frac{2\pi y}{\Lambda} - S_3 \sin\frac{2\pi y}{\Lambda}\right] \end{cases} \quad (3)$$

and can be uniquely reconstructed by following the standard fringe analysis scheme [48].

To validate the proposed single-shot compressive spatiospectral polarimetry technique, we use a polarizer and a quarter wave plate to construct different spatially and spectrally uniform polarization states described by Stokes vectors on the surface of the Poincaré sphere $(S_1/S_0, S_2/S_0, S_3/S_0)$. As shown in Fig. 1c, the ground truth Stokes vectors are labeled in black circles. Meanwhile, we have measured the corresponding 3D Stokes vectors in a single shot and averaged them spatiospectrally in each case (solid dots). The averaged Stokes parameters are tabulated and agree well with the ground truths, justifying the single-shot compressive spatiospectral polarimetry.

Results

The 3D snapshot of a linearly polarized THz electromagnetic wave packet

Now we demonstrate the reconstruction of an *x*-polarized THz electromagnetic wave packet from the 3D spatially- and spectrally-varied polarization state of the optical probe. The input polarization state of the optical probe is calibrated and uniformly set to $\left(S_1^{(\mathrm{In})}/S_0^{(\mathrm{In})}, S_2^{(\mathrm{In})}/S_0^{(\mathrm{In})}, S_3^{(\mathrm{In})}/S_0^{(\mathrm{In})}\right)$ = (-0.03, -0.40, 0.91). The *x*-polarization of the THz wave packet is obtained by driving the $LiNbO_3$ crystal with an *x*-polarized femtosecond laser pulse. As a result, the output 3D spatiospectral polarization state is modified from the input one, illustrated by clear variations of normalized Stokes parameters $\Delta S_i/S_0$ $(i = 1,2,3)$ in Figure 2(a-c), respectively. The maximum variations of these normalized Stokes parameters in the central spatial region approach 0.48, 0.17, and 0.20, respectively (Figure 2d). The central region size is 3.7 mm and consistent with the THz spot size at the electro-optic crystal, which has been independently measured through the common EO method.

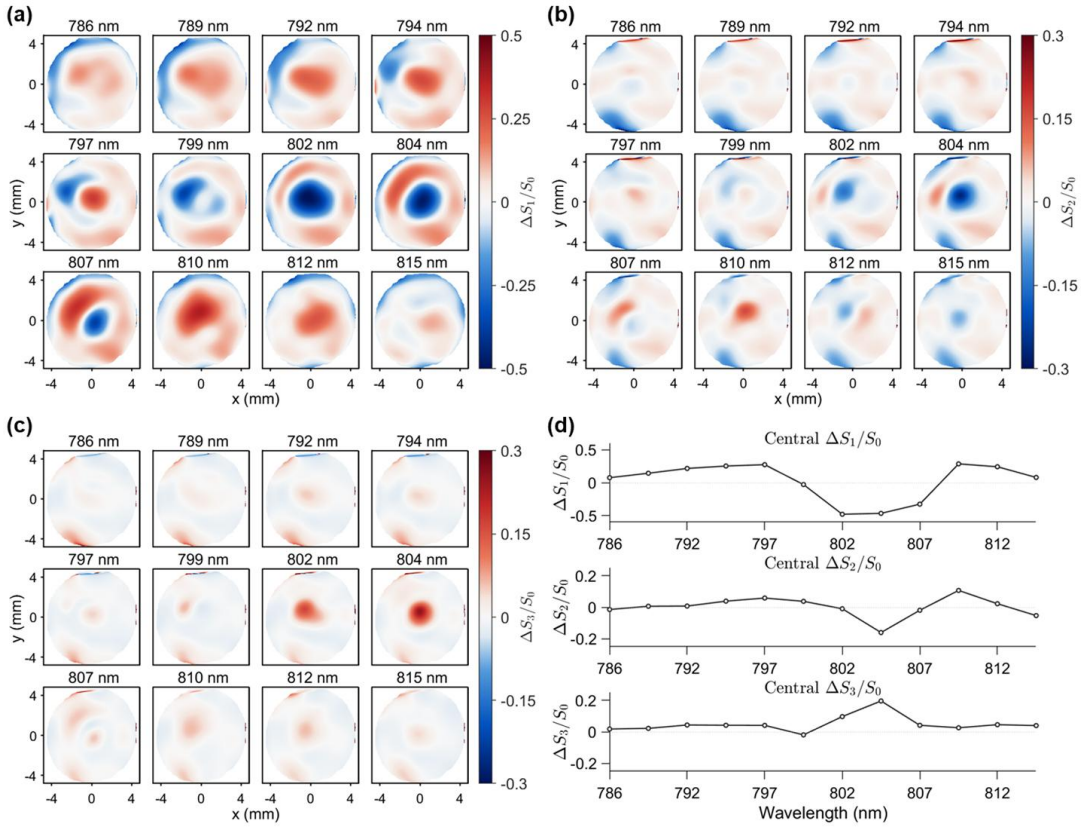


Figure 2. The normalized spatiospectral Stokes parameter variations of the probe laser pulse induced by an x-polarized THz wave packet. a-c. Spatial profiles of the normalized Stokes parameter variations $\Delta S_1/S_0$ **(a)**, $\Delta S_2/S_0$ **(b)** and $\Delta S_3/S_0$ **(c)** of the probe laser pulse at different wavelengths from 786 nm to 815 nm. **d**. The wavelength-dependent normalized Stokes parameter variations at the spatially central position.

Based on the reconstructed $S_i^{(\mathrm{Out})}/S_0^{(\mathrm{Out})}$ $(i = 1, 2, 3)$ in the spatial-spectral domain, we first directly map them to the spatiotemporal domain using the linear chirp relation $t = a_\lambda(\lambda - \lambda_0)$. With the 3D spatiotemporal polarization information of the optical probe, the optical-axis direction $\psi(x, y, t)$ and phase retardation $\Delta(x, y, t)$ of the THz-induced transient wave plate are obtained according to Eq. (2), and the transverse electric field components $E_x(x, y, t)$ and $E_y(x, y, t)$ are finally deduced based on Ref. [42]. The longitudinal field strength $E_z(x, y, t)$ is calculated based on the Poisson equation.

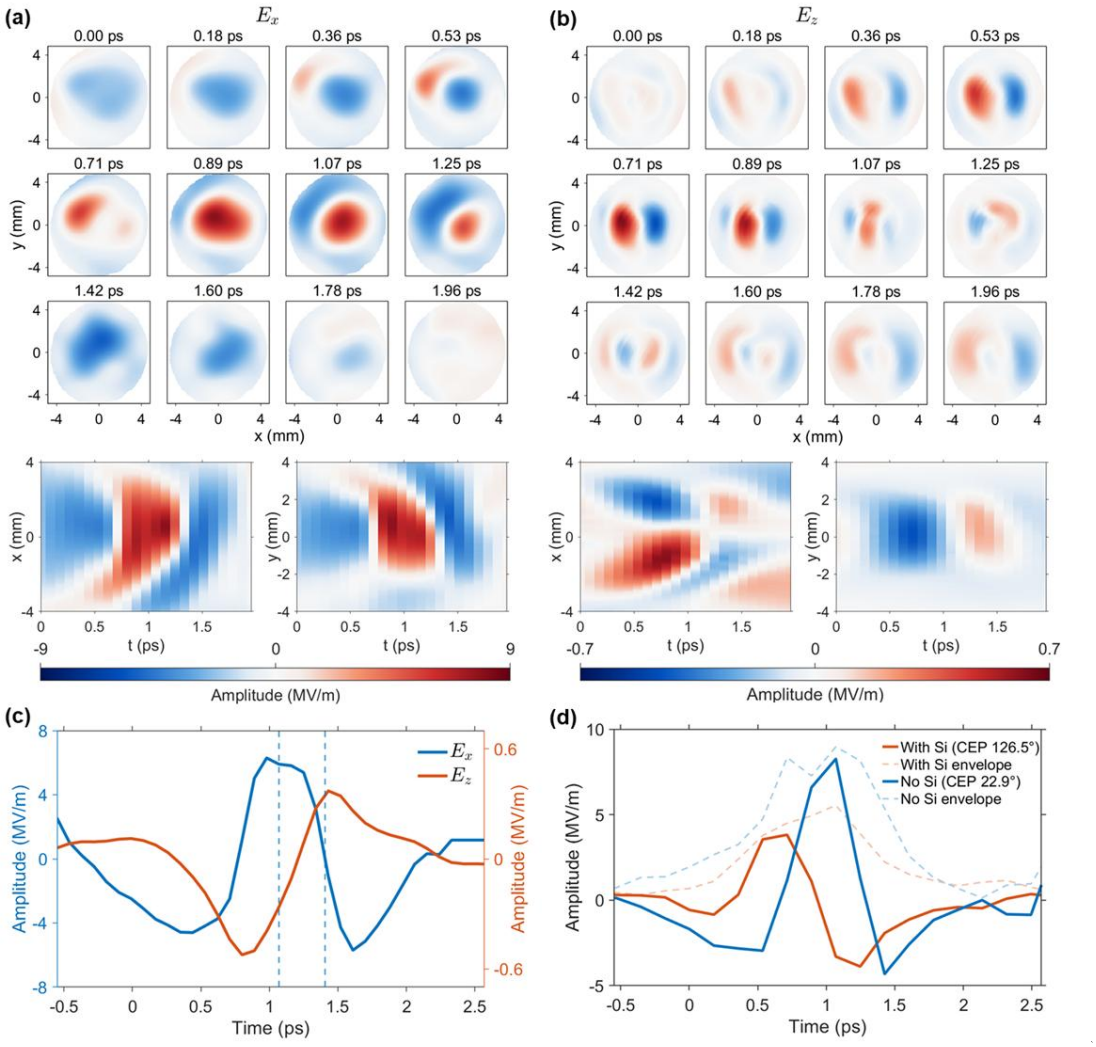


Figure 3. Single-shot 3D snapshot of the x-polarized THz electromagnetic wave packet. a. Spatial profiles of the THz transverse electric field component E_x at 12 consecutive times with an interval of 178 fs. The lower panels show the corresponding x-t and y-t spatiotemporal electric field profile sections extracted at $y = 0$ mm and $x = 0$ mm, respectively. **b.** Corresponding spatial profiles of the THz longitudinal electric field component E_z, together with the corresponding $x - t$ and $y - t$ spatiotemporal electric field profile sections extracted at $y = 0$ mm and $x = 1$ mm, respectively. **c.** The comparison between the temporal waveforms of the THz transverse E_x (blue) and longitudinal E_z (red) electric fields at $(x, y) = (1,0)$ mm. The vertical dashed lines indicate the temporal positions of the peak and the subsequent zero crossing of E_x, respectively. **d.** The comparison between the temporal waveforms of the THz transverse electric fields with (red solid) and without (blue solid) a 5-mm-thick silicon plate, which introduces a shift of carrier envelope phase. The dashed lines show corresponding envelope functions.

Figure 3a shows the 3D spatiotemporal snapshot of the transverse electric field strength $E_x(x, y, t)$. In the upper panels, twelve consecutive frames of x-y spatial

profiles are efficiently obtained from $t = 0$ to 2.0 ps with a time interval of 178 fs, which is close to the ~214 fs temporal resolution of the system due to the time-frequency mapping scheme (see Supplementary Document, Section 3). In the central region, the electric field evolves over approximately one and a half periods within ~2 ps, corresponding to a temporal period of ~1.26 ps and a central frequency of 0.79 THz. The maximum field strength is 8.3 MV/m, which can efficiently introduce the electro-optic effect in the ZnTe EO crystal. In the surrounding negative-x and positive-y region, the electric field with an opposite sign to that in the center is observed. To understand such a spatial distribution of the transverse electric field, we have taken the spatiotemporal x-t section at $y = 0$ and the y-t section at $x = 0$ in Figure 3a bottom left and right panels, respectively. Both spatiotemporal profiles in the x-t and y - t sections show concave-curved wavefront structures, indicating a slightly converging beam geometry of the incident THz wave packet. The slight asymmetric distributions of the electric field relative to the axis can be quantitatively described by a maximum time advance of ~0.3 ps of the wavefront on the edge relative to that in the center, implying a small angle of several milliradians between the propagation directions of the THz wave packet and the optical probe pulse.

The 3D snapshot of the longitudinal electric field strength $E_z(x, y, t)$ is shown in Figure 3b, similar to Figure 3a, including x-y spatial profiles at different times in the upper panel and the spatiotemporal x-t and y-t sections at $y = 0$ and $x = 1$, respectively, in the bottom left and right panels. Compared to the transverse field, the longitudinal field strength is one order of magnitude lower due to the gradual THz focusing geometry with the f-number of ~7. Along the polarization plane, the x-t spatiotemporal profile (Figure 3b bottom left panel) shows essential features of the longitudinal field component of an *x*-polarized electromagnetic wave packet: the field strength is null along the axis ($x = 0$) and has an antisymmetric off-axial spatial feature at any time. However, the y-t spatiotemporal E_z profile (Figure 3b bottom right panel) has no such antisymmetric spatial feature; instead, it is similar to the x-t spatiotemporal E_x profile (Figure 3a bottom right panel). However, they are different in the absolute carrier envelope phase (CEP) by $\pi/2$, as shown in the detailed

comparison between the transverse and longitudinal electric field waveforms in the off-axial spatial position $(x, y) = (1,0)$ mm (Figure 3c). All these observations are consistent with the longitudinal electric field theory for a focused electromagnetic wave [49].

Compared to the single-shot 3D vectorial complex amplitude visualization [2,3], the snapshot of a 3D electromagnetic wave packet provides the absolute CEP information. We have introduced a carrier-envelope phase shift to the incident THz wave packet by transmitting it through a 5-mm-thick silicon plate, so the difference between the phase and group velocities would shift the absolute phase of the THz field. Figure 3d shows the temporal field strength profiles of the THz wave packets in the center with (red solid line) and without (blue solid line) the silicon plate; meanwhile, the corresponding temporal envelope profiles are extracted through a Fourier transformation and spectral filtering procedure (red and blue dashed lines). Two obvious differences are observed. First, the field strength measured with the silicon plate is nearly half weaker than that without it, because the reflection on the interfaces and the absorption in the bulk silicon material attenuate the THz wave packet. Second, the THz waveform without the silicon plate is almost cosine-shaped with the accurate CEP of 22.9°, while that with the silicon plate is negatively sine-shaped with the CEP of 126.5°. Therefore, a single-shot 3D snapshot of the THz wave packet provides all necessary information describing an electromagnetic wave, including transverse and longitudinal electric field waveforms as well as the absolute carrier-envelope phase.

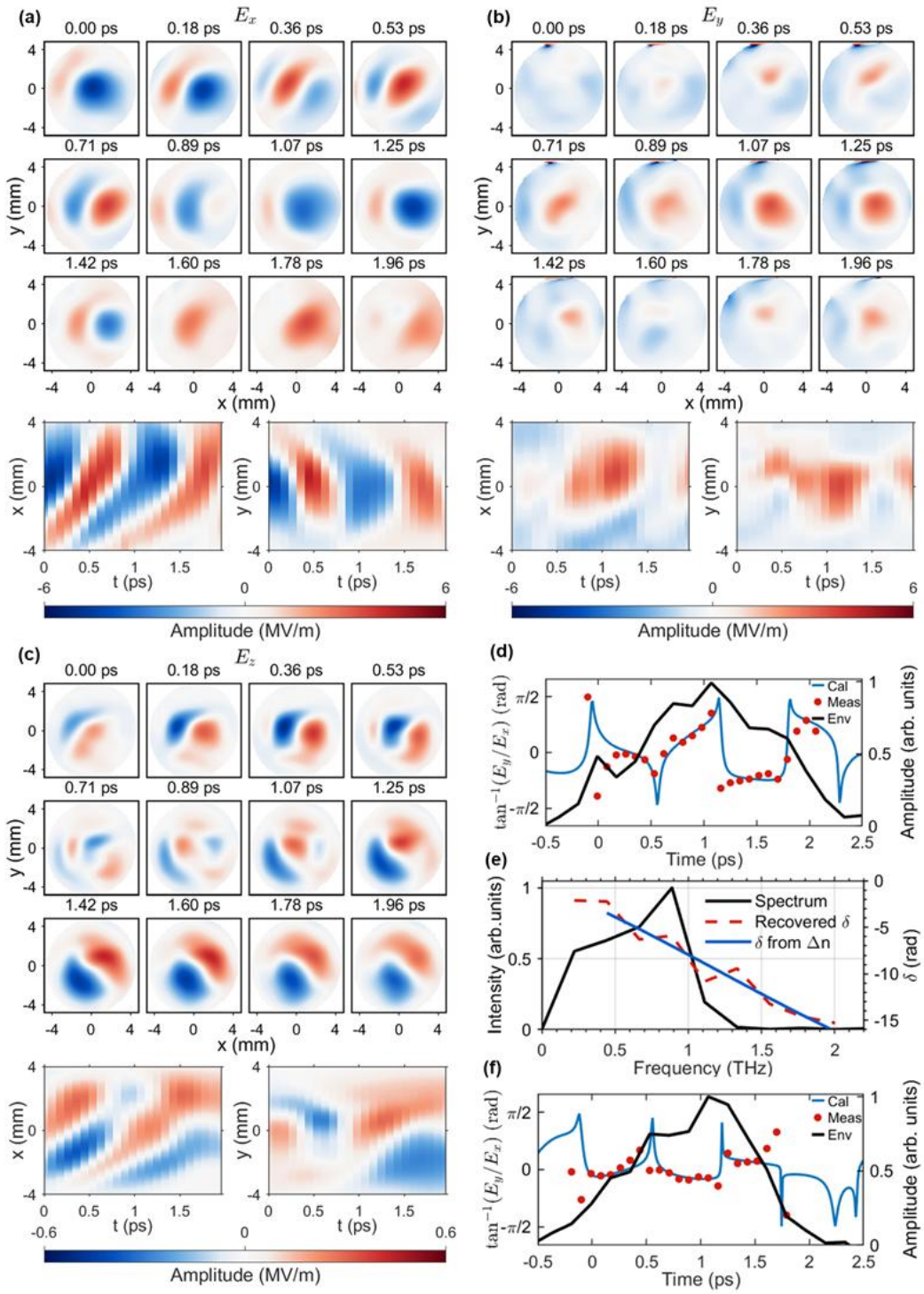


Figure 4. Single-shot 3D snapshot of a vectorial THz electromagnetic wave packet with a complicated spatiotemporal field distribution. a-c. Spatial profiles of the THz electric field components E_x, E_y and E_z, respectively, at 12 consecutive times with an interval of 178 fs in the upper panels. The lower panels show the corresponding x-t and y-t spatiotemporal electric field profile sections extracted at $y = 0$ mm and $x = 0$ mm, respectively. **d.** The measured temporal evolution of the transverse field polarization direction $\tan^{-1}(E_y/E_x)$ at the spatial center (red dots) when the x-polarized THz wave packet transmits through a quartz plate with an optical-axis angle

of 45°. As a comparison, the calculated $\tan^{-1}(E_y/E_x)$ is plotted in a blue solid line, and the corresponding field envelope is shown by the black solid line. Data points with a normalized field amplitude below 0.2 are excluded from the polarization-angle analysis. **e.** The measured frequency-resolved phase retardance δ induced by the quartz plate at an optical-axis angle of 45° (red dashed line) and the corresponding theoretical calculation (blue line). The measured THz spectrum is shown by the black solid line. **f.** Same as **d**, but the optical-axis angle of the quartz plate is 15°.

The 3D snapshot of a THz electromagnetic wave packet with spatiotemporally varying vectorial field distribution

Even just taking the transverse electric field into account, an electromagnetic wave can have a complicated 3D spatiotemporally varying distribution of the transverse electric field components E_x and E_y, so a complete 3D snapshot of an electromagnetic wave packet should be vectorially field-resolved. Compared to the experiments in the previous section for a linearly polarized THz wave packet, both the E_x and E_y components of an arbitrarily polarized THz wave introduce transient birefringence in the electro-optic crystal, so the one-to-one correspondence between the 3D vectorial THz field distribution $\mathbf{E}(x,y,t)$ and the transient wave plate parameters $\psi(x,y,t)$ and $\Delta(x,y,t)$ should be guaranteed (see Supplementary Document, Section 1). In the experiment, the initially *x*-polarized THz wave packet transmits through an 8-mm-thick crystalline quartz plate (x-cut), which can be rotated for different optical-axis angles. Due to the broadband nature of the single-cycle THz wave packet, the significant spectral dispersion induces different phase retardations between ordinary (*o*) and extraordinary (*e*) polarization components of the THz wave packet in each spectral channel, resulting in distinct spatiotemporal evolutions of E_x and E_y after transmission through the quartz plate.

We first set the optical-axis angle of the quartz plate to 45°. Figure 4a-c show the reconstructed electric field profiles of $E_x(x,y,t)$, $E_y(x,y,t)$, and $E_z(x,y,t)$, respectively, including the *x*-*y* spatial profiles at twelve consecutive time frames over 2 ps in the upper panel and *x*-*t* and *y*-*t* spatiotemporal profile sections in the bottom panels. One of the transverse electric field components E_x shows a clear feature of one and a half cycles with a concave and tilted wavefront, similar to the *x*-polarized THz wave

packet shown in Figure 3a. However, the optical-cycle feature in the other transverse electric field component E_y (Figure 4b) becomes ambiguous because of the rapidly evolving polarization property of the vectorial THz wave packet. Therefore, E_x and E_y together illustrate a time-varying transverse electric field direction, which can be marked by the angle of $\tan^{-1}(E_y/E_x)$. For the longitudinal electric field E_z, which is reconstructed based on the Poisson equation (Figure 4c), the off-axial antisymmetric spatial distribution is still approximately valid, but the on-axial field strengths at different times are no longer zero due to the complicated vectorial nature of the THz wave packet.

To justify the 3D snapshot of the complicated vectorial THz wave packet, we have lined out the time-varying transverse electric field polarization property at the spatial center $(x, y) = (0,0)$ mm and compared it with theoretical calculations. Figure 4d shows the experimentally retrieved transverse field direction $\tan^{-1}(E_y/E_x)$ (red dots), together with the field amplitude envelope (black solid line), illustrating an ultrafast rotation of the transverse field vector within hundreds of femtoseconds. Meanwhile, the spectral phase retardation differences between the *o*- and *e*-polarization components of the THz wave packet are calculated by taking Fourier-transformation to the temporal electric field profiles (Figure 4e, red dashed line). To justify the measurement, we have looked up the THz refractive index of crystalline quartz in the literature [50] and theoretically calculated the spectral *o*-*e* phase retardation difference (Fig. 4e, blue solid line), which is consistent with the experimental result. Using the measured THz complex amplitude in the spectral domain (Figure 4e, black solid line) and the theoretically calculated spectral *o*-*e* phase retardations, we calculate the transverse electric field direction $\tan^{-1}(E_y/E_x)$ in the temporal domain (Figure 4d, blue solid line), which is again consistent with the experimental result.

Furthermore, we have rotated the quartz crystal angle to 15°, obtaining a 3D snapshot of the THz wave packet with different spatiotemporally varying electric field components. Figure 4f shows the measured $\tan^{-1}(E_y/E_x)$ at the spatial center with the corresponding theoretical calculation, together with the temporal field envelope. The measured transverse field direction result is consistent with the corresponding

theoretical calculation again. Therefore, the 3D THz snapshot can faithfully reproduce the vectorial nature of any electromagnetic wave packet.

Discussion

In summary, we have demonstrated a full-Stokes compressive spatiospectral polarimetry technique to capture the 3D spatial and spectral polarization state profile of an arbitrary laser pulse. By sampling a THz wave packet in an electro-optic crystal with a chirped ultrafast laser pulse, a 3D spatiospectral snapshot of the electromagnetic wave packet in the THz spectral range is taken in a single shot. The 3D snapshot has revealed all necessary information describing the electromagnetic wave packet, including the three electric field components E_x, E_y and E_z, the carrier-envelope phase, and the complete 3D spatiotemporal distribution of all these physical quantities. Therefore, after more than 160 years since Maxwell predicted the electromagnetic wave, one can finally visualize an electromagnetic wave packet with its holistic information in a single exposure.

The significance of capturing the 3D THz wave packet snapshot is never limited to a fundamental science problem of "seeing" an electromagnetic wave or visualizing a solution to Maxwell's equations, but sheds light on a possible paradigm of sensing light for enormous applications. For example, obtaining complete THz wave packet information reinforces conventional ultrafast THz spectroscopy with spatially resolved new degrees of freedom such as dielectrically or magnetically anisotropic properties of materials and field-induced intra-band electron dynamics [51-54]. Even based on coherent transition radiation and distorted Coulomb field due to a relativistic electron bunch, a 3D THz wave packet snapshot provides novel diagnostics of ultrafast electron bunches in accelerator facilities for advanced free-electron laser sources [55-57].

Finally, we expect such a 3D electromagnetic wave packet snapshot to be extended beyond the current THz spectral regime, towards infrared and even visible regimes. The basic logic of the proposed 3D electromagnetic wave packet snapshot is single-shot sampling of a low-frequency electromagnetic wave packet with a high-frequency laser pulse, and then completely characterizing the complex amplitude or the polarization state of the laser pulse in full dimensions and in a single shot. Following this track, even

a 3D near-infrared wave packet snapshot can be expected with a visible optical probe since electro-optic sampling of near-infrared laser fields has been demonstrated [5-7]. Considering that the extreme ultraviolet ionization of laser field dressed atoms is a similar electric field sampling process [8-10], we would expect that advances in spatiotemporal attosecond pulse characterization, even in 3D, potentially benefit the realization of a 3D visible or violet wave packet snapshot [58-60].

Methods

Generation of the THz wave packet using a $LiNbO_3$ electro-optic crystal

The THz wave packets were generated through a tilted-pulse-front optical rectification scheme in a lithium niobate ($LiNbO_3$) crystal. A near-infrared pump pulse (pulse energy 4.7 mJ, wavelength 800 nm) is spectrally filtered by a bandpass filter (Thorlabs, FBH800-10) to obtain a spectral bandwidth of 24 nm (full width at half maximum, FWHM). Then the pump beam was incident on a blazed grating (1,800 lines mm^{-1}) at 35.3°, and the first diffraction order had a pulse-front tilt. The tilted pulse front was imaged into a $LiNbO_3$ prism with an apex angle of 62° using two cylindrical lenses with focal lengths of 25 cm and 15 cm, respectively, ensuring velocity matching between the optical pump pulse and the generated terahertz field as well as efficient broadband terahertz generation through the second-order optical rectification [45]. As a result, the THz pulse energy is optimized to 5.4 μJ at the crystal output and measured by a calibrated terahertz power meter (THz 5B-BL-DZ, Gentec-EO). The generated terahertz pulse was collimated and expanded using three off-axis parabolic mirrors with focal lengths of 10 cm, 5 cm, and 10 cm, respectively, then focused onto the ZnTe electro-optic crystal by a TPX lens (focal length 7.5 cm).

The 3D spatiospectral interferogram reconstruction using the TwIST algorithm

In the system, the 3D spatiospectral interferogram data cube ($\mathbf{X}$) was spatially encoded by the mask ($\mathbf{M}$), spectrally sheared by the prism ($\mathbf{S}$), and spectrally collected by the camera ($\mathbf{C}$), generating a two-dimensional image ($\mathbf{Y}$), so the whole measurement process can be expressed by a linear transformation

$$\mathbf{Y} = \mathbf{CSMX} = \mathbf{AX} \tag{4}$$

where $\mathbf{A} = \mathbf{CSM}$ is the transformation matrix. The compressive sensing algorithm of two-step iterative shrinkage/thresholding (TwIST) has been applied [47], solving the total-variation-regularized optimization problem

$$\widehat{\mathbf{X}} = \arg\min_{\mathbf{X}} \left\{ \frac{1}{2} \|\mathbf{Y} - \mathbf{AX}\|_2^2 + \tau \Phi_{\mathrm{TV}}(\mathbf{X}) \right\} \quad (5)$$

where the first term enforces consistency between the reconstructed data cube and the measured image, and $\tau = 0.15$ controls the strength of the regularization. Following the conventional formulation for coded-aperture spectral imaging, the isotropic spatial total variation was defined as

$$\Phi_{\mathrm{TV}}(\mathbf{A}) = \sum_k \sum_{i,j} \sqrt{\left[\left(A_{i+1,j,k} - A_{i,j,k} \right)^2 + \left(A_{i,j+1,k} - A_{i,j,k} \right)^2 \right]} \quad (6)$$

where i and j denote the two spatial coordinates and k denotes the spectral channel. The total-variation term suppresses spatial fluctuations while preserving the principal spatial structures in each spectral slice.

References

[1] Maxwell, J. C. A dynamical theory of the electromagnetic field. *Philos. Trans. R. Soc. Lond.* **155**, 459–512 (1865).

[2] Hu, Y. et al. High-dimensional one-shot optical field compressive sensing of structured light. *Nat. Commun.* **16**, 7370 (2025).

[3] Howard, S. et al. Single-shot spatiotemporal vector field measurements of petawatt laser pulses. *Nat. Photon.* **19**, 898–905 (2025).

[4] Pariente, G., Gallet, V., Borot, A., Gobert, O. & Quéré, F. Space–time characterization of ultra-intense femtosecond laser beams. *Nat. Photon.* **10**, 547–553 (2016).

[5] Keiber, S. et al. Electro-optic sampling of near-infrared waveforms. *Nat. Photon.* **10**, 159–162 (2016).

[6] Mamaikin, M. et al. Electric-field-resolved near-infrared microscopy. *Optica* **9**, 616–622 (2022).

[7] Ridente, E. et al. Electro-optic characterization of synthesized infrared-visible light

fields. *Nat. Commun*. **13**, 1111 (2022).

[8] Goulielmakis, E. et al. Direct measurement of light waves. *Science* **305**, 1267–1269 (2004).

[9] Kienberger, R. et al. Atomic transient recorder. *Nature* **427**, 817–821 (2004).

[10] Park, S. B. et al. Direct sampling of a light wave in air. *Optica* **5**, 402–408 (2018).

[11] Matselyukh, D. T. et al. Petahertz polarimetry using tunneling ionization. *Ultrafast Sci.* **5**, 0113 (2025).

[12] Liu, Y., Beetar, J. E., Nesper, J., Gholam-Mirzaei, S. & Chini, M. Single-shot measurement of few-cycle optical waveforms on a chip. *Nat. Photon.* **16**, 109–112 (2022).

[13] Truong, T.-C. et al. Scanless laser waveform measurement in the near-infrared. *APL Photonics* **10**, 016101 (2025).

[14] Tonouchi, M. Cutting-edge terahertz technology. *Nat. Photon.* **1**, 97–105 (2007).

[15] Nagatsuma, T., Ducournau, G. & Renaud, C. C. Advances in terahertz communications accelerated by photonics. *Nat. Photon.* **10**, 371–379 (2016).

[16] Mittleman, D. M. Twenty years of terahertz imaging [Invited]. *Opt. Express* **26**, 9417–9431 (2018).

[17] Li, X., Li, J., Li, Y., Ozcan, A. & Jarrahi, M. High-throughput terahertz imaging: progress and challenges. *Light Sci. Appl.* **12**, 233 (2023).

[18] Ulbricht, R., Hendry, E., Shan, J., Heinz, T. F. & Bonn, M. Carrier dynamics in semiconductors studied with time-resolved terahertz spectroscopy. *Rev. Mod. Phys.* **83**, 543–586 (2011).

[19] Lloyd-Hughes, J. & Jeon, T.-I. A review of the terahertz conductivity of bulk and nano-materials. *J. Infrared Millim. Terahertz Waves* **33**, 871–925 (2012).

[20] Zhang, D. et al. Segmented terahertz electron accelerator and manipulator (STEAM). *Nat. Photon.* **12**, 336–342 (2018).

[21] Ying, J. et al. High gradient terahertz-driven ultrafast photogun. *Nat. Photon.* **18**, 758–765 (2024).

[22] Li, X. et al. Plasmonic photoconductive terahertz focal-plane array with pixel super-resolution. *Nat. Photon.* **18**, 139–148 (2024).

460 [23] Brahm, A. et al. Multichannel terahertz time-domain spectroscopy system at 1030
461 nm excitation wavelength. *Opt. Express* **22**, 12982–12993 (2014).
462 [24] Wu, Q. & Zhang, X.-C. Free-space electro-optic sampling of terahertz beams. *Appl.*
463 *Phys. Lett.* **67**, 3523–3525 (1995).
464 [25] Roussel, E. et al. Phase Diversity Electro-optic Sampling: A new approach to
465 single-shot terahertz waveform recording. *Light Sci. Appl.* **11**, 14 (2022).
466 [26] Jiang, Z. & Zhang, X.-C. Single-shot spatiotemporal terahertz field imaging. *Opt.*
467 *Lett.* **23**, 1114–1116 (1998).
468 [27] Shan, J. et al. Single-shot measurement of terahertz electromagnetic pulses by use
469 of electro-optic sampling. *Opt. Lett.* **25**, 426–428 (2000).
470 [28] Kim, K. Y., Yellampalle, B., Taylor, A. J., Rodriguez, G. & Glownia, J. H. Single-
471 shot terahertz pulse characterization via two-dimensional electro-optic imaging with
472 dual echelons. *Opt. Lett.* **32**, 1968–1970 (2007).
473 [29] Zhao, J., E, Y., Williams, K., Zhang, X.-C. & Boyd, R. W. Spatial sampling of
474 terahertz fields with sub-wavelength accuracy via probe-beam encoding. *Light Sci.*
475 *Appl.* **8**, 55 (2019).
476 [30] Zanotto, L. et al. Time-domain terahertz compressive imaging. *Opt. Express* **28**,
477 3795–3802 (2020).
478 [31] Guerboukha, H., Nallappan, K. & Skorobogatiy, M. Exploiting k-space/frequency
479 duality toward real-time terahertz imaging. *Optica* **5**, 109–116 (2018).
480 [32] Dong, J., You, P., Tomasino, A., Yurtsever, A. & Morandotti, R. Single-shot
481 ultrafast terahertz photography. *Nat. Commun.* **14**, 1704 (2023).
482 [33] Castro-Camus, E. et al. Polarization-sensitive terahertz detection by multicontact
483 photoconductive receivers. *Appl. Phys. Lett.* **86**, 254102 (2005).
484 [34] Makabe, H., Hirota, Y., Tani, M. & Hangyo, M. Polarization state measurement of
485 terahertz electromagnetic radiation by three-contact photoconductive antenna. *Opt.*
486 *Express* **15**, 11650–11657 (2007).
487 [35] Oguchi, K., Yasumatsu, N. & Watanabe, S. Polarization detection of terahertz
488 radiation via the electro-optic effect using zinc blende crystal symmetry. *J. Opt. Soc.*
489 *Am. B* **31**, 3170–3180 (2014).

490 [36] Yasumatsu, N. & Watanabe, S. Precise real-time polarization measurement of
491 terahertz electromagnetic waves by a spinning electro-optic sensor. *Rev. Sci. Instrum.*
492 **83**, 023104 (2012).
493 [37] Van der Valk, N. C. J., Van der Marel, W. A. M. & Planken, P. C. M. Terahertz
494 polarization imaging. *Opt. Lett.* **30**, 2802–2804 (2005).
495 [38] Lenz, M. & Musumeci, P. Single-shot electro-optic sampling with arbitrary
496 terahertz polarization. *Photon. Res.* **13**, 1736–1746 (2025).
497 [39] Lin, Q. et al. Single-shot terahertz polarization detection based on terahertz time-
498 domain spectroscopy. *Photon. Res.* **10**, 1374–1379 (2022).
499 [40] Harris, Z. B., Xu, K. & Arbab, M. H. A handheld polarimetric imaging device and
500 calibration technique for accurate mapping of terahertz Stokes vectors. *Sci. Rep.* **14**,
501 17714 (2024).
502 [41] Zhang, Z.-K. et al. Deep learning-enabled ultra-broadband terahertz high-
503 dimensional photodetector. *Nat. Commun.* **16**, 8133 (2025).
504 [42] Chen, Q., Tani, M., Jiang, Z. & Zhang, X.-C. Electro-optic transceivers for
505 terahertz-wave applications. *J. Opt. Soc. Am. B* **18**, 823–831 (2001).
506 [43] Tang, H., Marquez, M., Men, T., Hu, Y., Tang, W., Liang, J. & Li, Z. Temporal
507 resolution of ultrafast compressive imaging using a single-chirped optical probe. *Opt.*
508 *Lett.* **48**, 6080–6083 (2023).
509 [44] Kim, K. Y., Alexeev, L. & Milchberg, H. M. Single-shot supercontinuum spectral
510 interferometry. *Appl. Phys. Lett.* **81**, 4124 (2002).
511 [45] Hirori, H., Doi, A., Blanchard, F. & Tanaka, K. Single-cycle terahertz pulses with
512 amplitudes exceeding 1 MV/cm generated by optical rectification in $LiNbO_3$. *Appl.*
513 *Phys. Lett.* **98**, 091106 (2011).
514 [46] Wagadarikar, A., John, R., Willett, R. & Brady, D. Single disperser design for
515 coded aperture snapshot spectral imaging. *Appl. Opt.* **47**, B44–B51 (2008).
516 [47] Bioucas-Dias, J. M. & Figueiredo, M. A. T. A new TwIST: two-step iterative
517 shrinkage/thresholding algorithms for image restoration. *IEEE Trans. Image Process.*
518 **16**, 2992–3004 (2007).
519 [48] Takeda, M., Ina, H. & Kobayashi, S. Fourier-transform method of fringe-pattern

analysis for computer-based topography and interferometry. *J. Opt. Soc. Am.* **72**, 156–160 (1982).

[49] Winnerl, S., Hubrich, R., Mittendorff, M., Schneider, H. & Helm, M. Universal phase relation between longitudinal and transverse fields observed in focused terahertz beams. *New J. Phys.* **14**, 103049 (2012).

[50] Castro-Camus, E. & Johnston, M. B. Extraction of the anisotropic dielectric properties of materials from polarization-resolved terahertz time-domain spectra. *J. Opt. A: Pure Appl. Opt.* **11**, 105206 (2009).

[51] Schubert, O. et al. Sub-cycle control of terahertz high-harmonic generation by dynamical Bloch oscillations. *Nat. Photon.* **8**, 119–123 (2014).

[52] Langer, F. et al. Lightwave-driven quasiparticle collisions on a subcycle timescale. *Nature* **533**, 225–229 (2016).

[53] Cheng, B. et al. Efficient terahertz harmonic generation with coherent acceleration of electrons in the Dirac semimetal Cd_3As_2. *Phys. Rev. Lett.* **124**, 117402 (2020).

[54] Chen, X. & Pickwell-MacPherson, E. An introduction to terahertz time-domain spectroscopic ellipsometry. *APL Photonics* **7**, 071101 (2022).

[55] Huang, K. et al. Electro-optic 3D snapshot of a laser wakefield accelerated kilo-ampere electron bunch. *Light Sci. Appl.* **13**, 84 (2024).

[56] Ota, M., Kan, K., Komada, S. et al. Ultrafast visualization of an electric field under the Lorentz transformation. *Nat. Phys.* **18**, 1436–1440 (2022).

[57] LaBerge, M. et al. Revealing the three-dimensional structure of microbunched plasma-wakefield-accelerated electron beams. *Nat. Photon.* **18**, 952–959 (2024).

[58] Chopineau, L. et al. Spatio-temporal characterization of attosecond pulses from plasma mirrors. *Nat. Phys.* **17**, 968–973 (2021).

[59] Kim, K., Zhang, C., Shiner, A. et al. Manipulation of quantum paths for space–time characterization of attosecond pulses. *Nat. Phys.* **9**, 159–163 (2013).

[60] Yan, M., Hu, Y., Wei, Z. & Li, Z. 3D characterization of spatiotemporally coupled high harmonic attosecond pulses. *Laser Photon. Rev.* **19**, 2401675 (2025).

Acknowledgement This work is financially supported by the National Key Research and Development Program of China (No. 2024YFB4607900), the National Natural Science Foundation of China (No. 12235005, 12275099, 12275249), Major Technological Innovation Program of HUST (No. 2025ZDKJCX09).

Supplementary Files

This is a list of supplementary files associated with this preprint. Click to download.

- SupplementaryTHz260907final.docx